ACADEMIA QUANTUM

Technical Note
Published: 2025-04-30
https://doi.org/10.20935/AcadQuant7690

Design of a quantum diamond microscope with efficient scanning confocal readout

Daniel G. Ang[1,*,†], Jiashen Tang[1,2,†], Ronald L. Walsworth[1,2,3,*]

Academic Editors: Yuhua Duan

Abstract

In this paper we introduce the light-sheet confocal quantum diamond microscope (LC-QDM) for widefield 3D quantum sensing with efficient confocal readout. The LC-QDM leverages light-sheet illumination and laser scanning confocal methods to enable high-resolution, high-speed 3D measurements with nitrogen-vacancy (NV) defects in diamond, combining the best of widefield and confocal modalities in a single device and eliminating the need for thin-NV-layer diamond chips. We perform simulations and measurements of NV initialization and readout times to model the anticipated performance of the LC-QDM compared to existing QDM designs. Our findings show that the LC-QDM will provide significant advantages for applications requiring limited laser power.

Keywords: *quantum diamond microscope, quantum sensing, nitrogen-vacancy centers, NV diamond, confocal microscopy*

Citation: Ang DG, Tang J, Walsworth RL. Design of a quantum diamond microscope with efficient scanning confocal readout. *Academia Quantum* 2025;2. https://doi.org/10.20935/AcadQuant7690

1. Introduction

The quantum diamond microscope (QDM) is an established quantum sensing technology that images properties of interest such as magnetic fields, strain, and temperature. The QDM provides a wide field of view (FOV), high spatial resolution, and operation in ambient conditions [1–3]. These features have enabled diverse applications in fields such as material science [4], life sciences [5–8], geology [9–12], microelectronics analysis [13–16], and efforts at dark matter detection [17–19]. The QDM utilizes an ensemble of negatively-charged nitrogen-vacancy (NV) centers in diamond for quantum sensing [20]. Illumination with green (typically 532 nm) laser light is used for NV initialization and readout of the sensor information encoded in the NV photoluminescence (PL, ∼600−800 nm). QDM spatial resolution is typically determined by the smallest volume of NV diamond that can be optically differentiated during readout (hereinafter referred to as the sensing voxel) [21]. This volume represents the smallest 3D unit of NV centers that can be independently measured. Beyond spatial resolution, accurate source reconstruction also depends on minimizing the distance between the sample and NV sensors [22, 23].

To achieve ∼1 μm lateral resolution in a QDM, a high-magnification imaging system with a dense camera pixel array is typically employed [2]. This setup resolves NV sensing voxels in a 2D plane near the sample at the optical diffraction limit. However, because a camera-based imaging system lacks optical Z-sectioning, a thin NV ensemble layer (on the nano- to micron-scale) is required to prevent QDM image blurring. Fabricating layered NV diamond chips requires advanced techniques, such as ion implantation or chemical vapor deposition (CVD) at the surface of an existing diamond substrate [1], whereas commercially available quantum-grade diamond chips typically contain NV centers throughout the entire ∼0.5 mm-thick bulk diamond substrate [24, 25]. Additionally, a layered diamond chip limits quantum sensing to the active NV layer. This restricts quantum sensing to a single plane, rendering it unsuitable for applications like gradiometry and others that require flexibility in the placement of the sensing layer [18, 26, 27].

An alternative method to achieve micron-scale QDM resolution is point-by-point detection with a scanning confocal system, which enables readout from each diffraction-limited sensing voxel using a pinhole to reject out-of-focus light [28, 29]. However, moving the interrogation point with galvo mirrors or translation stages introduces dead times ($\gg$1 ms) that far exceed the duration of the quantum sensing protocol (typically $<$1 ms, limited by the NV spin polarization time T_1). Recent QDM designs by Leibold et al. [30] and Cambria et al. [31] mitigate this problem by using a pair of acousto-optic modulators (AOMs) to rapidly scan the green laser, reducing the dead time to ∼100 ns. Nonetheless, these systems do not have a pinhole for Z-sectioning capability, and thus they cannot be used with commercial bulk diamond chips. Furthermore, Reference [30] utilizes a recurrent readout scheme where multiple sensing voxels are interrogated after applying a global microwave (MW) control sequence applied to a wide FOV, resulting in increased readout duty cycle. In many QDM applications, much mo-

[1]Quantum Technology Center, University of Maryland, College Park, MD 20742, USA.
[2]Department of Physics, University of Maryland, College Park, MD 20742, USA.
[3]Department of Electrical Engineering and Computer Science, University of Maryland, College Park, MD 20742, USA.
*email: dga@umd.edu (D.G.A.); walsworth@umd.edu (R.L.W.)
†These authors contributed equally to this work.

re time is spent on NV spin initialization than on applying MW pulses, limiting the efficiency enhancement of this approach.

Here, we introduce a new QDM design that addresses these limitations by acquiring widefield images with a combination of optical-sectioning and highly-efficient confocal readout, thereby offering an upgrade over existing setups that are either limited by slow scanning speed, lack of Z-sectioning, or the need for NV-layered diamond chips. Hereafter, we refer to this system as a light-sheet QDM with confocal readout (LC-QDM).

The LC-QDM distinguishes itself from previous QDMs [1, 2, 30, 31] due to two innovations. First, a sheet of green light is employed to perform global initialization of all NV sensing voxels within a wide FOV. Second, rapid scanning confocal readout is performed by an optical system consisting of a pinhole and two pairs of AOMs. The LC-QDM's enhanced capabilities are applicable to many QDM applications utilizing a confocal setup, such as for 2D material characterization [4], strain imaging [19], super-resolution techniques [32–34], and ion-induced damage track detection for sensor optimization [35, 36] and fundamental physics applications [17, 18]. As shown in Section 3, the LC-QDM's efficient readout protocol offers a particular advantage for applications requiring limited laser power, such as bioimaging [5, 37], where reduced phototoxicity enables longer, more accurate mapping of magnetic fields in living cells.

2. Design of the LC-QDM

Figure 1 illustrates the LC-QDM's hardware setup, showcasing its core components. Initially, a green (532 nm) laser beam is shaped into a sheet and coupled through polished side facets of the diamond to illuminate and initialize NVs within the target FOV. Unlike conventional light-sheet systems [38], the thickness of the light-sheet in the LC-QDM is not critical, provided that the entire region of interest is uniformly illuminated. After a sufficient initialization time t_{init}^{LS} (typically 1–100 μs), the light-sheet is turned off.

Next, MW pulses are applied to the same NV population to perform quantum sensing protocols, delivered via a coaxial loop or resonator [39] to ensure field homogeneity across the FOV and compatibility with light-sheet illumination.

Finally, a second green laser beam (can be from the same source as the first beam), tightly focused by a microscope objective, is utilized to read out individual NV sensing voxels (~1 μm^3). A pair of AOMs is used to rapidly switch the position of the readout laser beam on the target FOV and generate a QDM image, similar to a laser scanning confocal system (**Figure 1b**). At each position, the readout laser dwells for a readout time t_{RO}^{conf} to capture a sufficient NV PL signal (typically 1–10 μs). The values of the initialization and readout times (t_{init}^{LS}, t_{RO}^{conf}) depend on the laser intensity (see Section 3.2). The resulting NV PL is collected by the same readout objective and propagates along unique paths for different NV voxels. A second pair of AOMs is introduced to descan the PL to maintain alignment with a fixed pinhole, thus allowing confocal readout. The drive radiofrequencies (RFs) of the two AOM pairs are calibrated to accurately point the path of the readout laser beam and maximize PL transmission through the pinhole. Synchronizing the RF signals for both AOM pairs minimizes dead time during beam movement and enables signal averaging for enhanced sensitivity.

3. Performance of the LC-QDM

3.1. Advantages of the LC-QDM

The LC-QDM enables high-speed, diffraction-limited confocal readout of NV PL from a bulk diamond sample, integrating key advantages of both scanning confocal and 2D widefield QDMs. A potential alternative system that integrates speed and optical sectioning is a light-sheet QDM without confocal readout [27, 38, 40]. However, achieving ~1 μm Z-resolution while maintaining a large FOV remains challenging with this system, with the best result

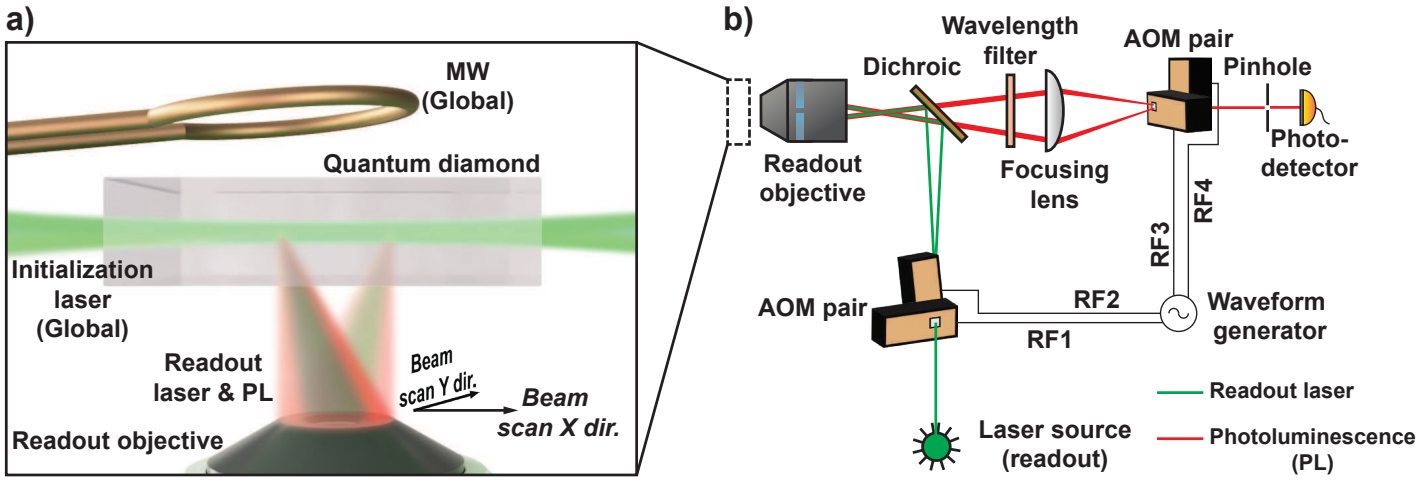


Figure 1 • Schematic of LC-QDM with high-speed, diffraction-limited readout. (**a**) Zoom-in view of the NV-diamond sensor head. A green laser beam, shaped into a wide sheet, illuminates a large area of the diamond to initialize NV spins across the entire FOV. A MW pulse sequence manipulates all NVs within the same FOV to perform quantum sensing. Optical readout of the NV sensor is performed point-by-point by focusing a second green laser beam through a microscope objective from below and collecting the resulting red NV PL from each sensing voxel. (**b**) Additional hardware components associated with NV readout. Two pairs of AOMs provide rapid control of the readout laser's propagation direction and the resulting location of induced NV red PL. Synchronizing the RF sources for each AOM pair enables precise XY-pointing of the readout laser and maintains alignment of the red PL with the pinhole, enabling optical sectioning and confocal NV PL readout.

to date achieving a Z-resolution of 14 μm [40]. Significant improvements with this approach will likely require the use of non-Gaussian beams for the light-sheet [38], significantly increasing optical complexity. Additionally, the light-sheet profile tends to be distorted when positioned close to the diamond surface due to diamond edge clipping. In contrast, the LC-QDM utilizes a confocal pinhole to accomplish Z-sectioning with a resolution ~1 μm (typical in confocal QDMs). As the sectioning is performed by the pinhole, a relatively simple, crude light-sheet suffices for global optical NV spin initialization.

In addition to optical Z-sectioning capability, the LC-QDM measurement protocol is more efficient than existing QDMs protocols. Using a light-sheet to initialize NVs in the entire FOV simultaneously allows a larger number of recurrent readouts within the NV T_1 limit compared to the method in Reference [30]. In particular, our protocol excels in applications with longer NV initialization and readout durations. These durations depend inversely on laser intensity, which can lead to practical constraints in real-world applications. For example, the intensity of a broad light-sheet laser beam can be limited by practically available laser power. Additionally, when a sample is placed directly on the top surface of the diamond chip, a common strategy to minimize sensor-to-sample standoff distance, the sample may be exposed to irradiation from the vertical readout beam. In applications such as magnetic imaging of biological cells [5, 7, 37], this exposure can induce phototoxic effects [41, 42]. Irradiation can also cause unwanted heating, compromising magnetometry of superconducting materials at cryogenic temperatures [43, 44]. Additionally, certain thin materials proposed for NV-based measurements are prone to photothermal degradation [45–47]. These effects limit the allowable laser power, potentially lengthening the initialization and readout times to several tens of microseconds, degrading the sensitivity of traditional QDMs and lengthening data collection. In these applications, LC-QDM readout is significantly more efficient than other QDMs. Furthermore, with the LC-QDM, the laser light enters the diamond from the side and does not interact directly with the sample, providing another advantage in bioimaging applications compared to confocal or total internal reflection illumination in widefield QDMs.

3.2. LC-QDM readout efficiency

To quantify the LC-QDM's projected readout efficiency advantage in more detail, we first measure the dependence of optical initialization and readout durations on laser intensity (**Figure 2**). The NV is an electronic spin-1 system that emits PL brighter in the $m_s = 0$ state compared to $m_s = \pm 1$ when undergoing optical pumping. See Refs. [1, 3] for detailed discussions of NV spin and optical properties, as well as commonly used NV measurement schemes and data analysis methods. We measure the NV PL contrast between $m_s = 0$ and $m_s = +1$ on a confocal QDM (no light-sheet) with the measurement protocol shown in **Figure 2a**. We use a CVD-grown diamond chip with the following properties: 3 mm × 3 mm × 0.5

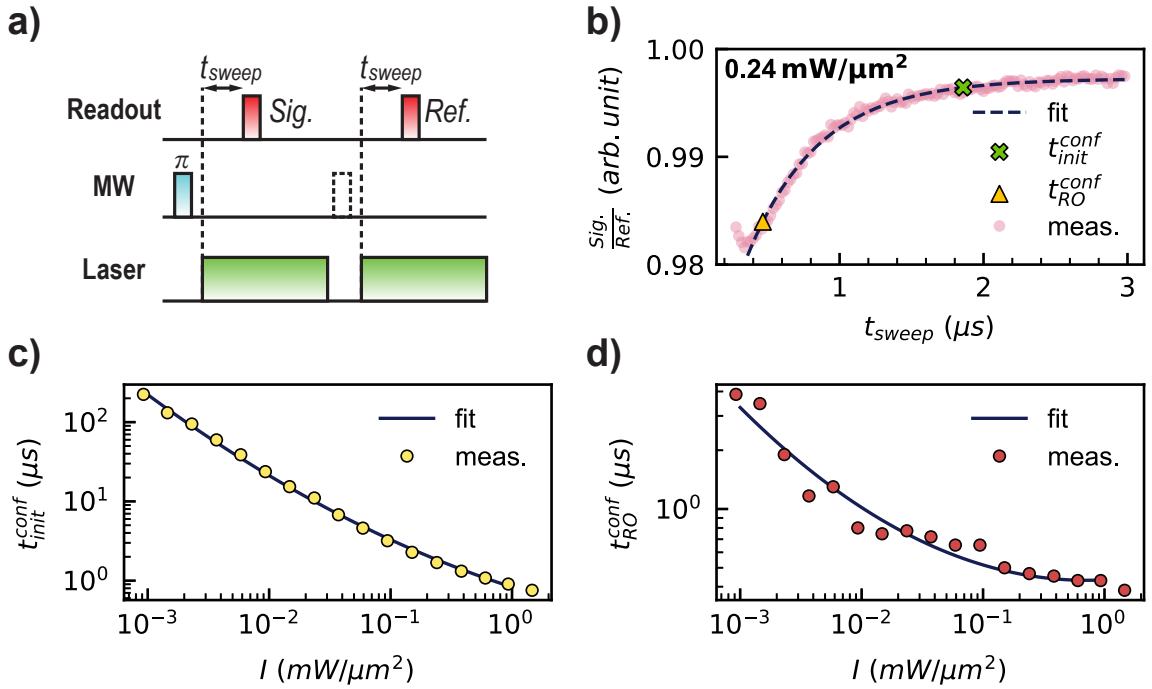


Figure 2 • Measured dependence of NV initialization and readout durations on laser intensity using a confocal QDM. (**a**) Measurement pulse sequence. Following a few μs laser pulses to initialize the NV spins to $m_s = 0$ and a MW π pulse to invert the NVs to $m_s = +1$, the readout data acquisition system records the instantaneous NV PL at a variable delay (t_{sweep}) after the laser is turned back on for another few μs. This signal PL measurement (Sig.) is followed by a reference PL measurement (Ref.) for the same delay but without the MW π pulse. Sweeping this delay enables simultaneous determination of optimal laser duration for NV spin-state readout and polarization. (**b**) Example measurement data employing pulse sequence in (**a**). See main text for discussion of the determination of NV spin readout t_{RO}^{conf} and initialization t_{init}^{conf} times. (**c**) Experimentally determined t_{init}^{conf} as a function of laser intensity I. Laser intensity is extracted from the measured power incident on the diamond divided by the confocal collection area. We assume the laser has a symmetric Gaussian profile. Uniform illuminance of the NVs is ensured by utilizing a confocal QDM with a pinhole whose size when projected to the objective plane is 2.5 × smaller than beam waist of the focused green laser. Data are fitted to a second-order polynomial function on a logarithmic scale. (**d**) Experimentally determined t_{RO}^{conf} as a function of laser intensity I, determined as in (**c**).

mm; 99.99% ^{12}C; bulk NV diamond with nominal [NV] = 0.3 ppm. From the measured dependence of contrast on the laser illumination duration t_{sweep} (**Figure 2b**), we determine i) t_{RO}^{conf} from the t_{sweep} value that maximizes the product of contrast and the square root of PL photon flux and ii) t_{init}^{conf} from the t_{sweep} value, for which contrast decays to $1/e^3$ of its peak value, effectively achieving $\gtrsim$95% initialization efficiency with an infinitely long laser pulse. Subsequently, we experimentally determine t_{init}^{conf} and t_{RO}^{conf} at different laser intensities I (**Figure 2c,d**). Fitting the data to exponentials allows us to extract the dependence of t_{RO}^{conf} and t_{RO}^{conf} on I.

Next, we apply these results to compare the projected readout efficiency of the LC-QDM to other scanning QDMs (**Figure 3a**). Readout efficiency can be quantified using the per-voxel sensitivity η to the parameter of interest (e.g., magnetic field), which relates signal-to-noise ratio (SNR) and total time t required to initialize and read out a single sensing voxel (including optical initialization and MW control sequence duration) as follows:

$$\eta = \frac{1}{SNR} \times \sqrt{t}. \tag{1}$$

The LC-QDM employs recurrent readout to amortize the time cost of initialization and MW control sequence. The number of maximum readouts is limited by NV T_1 due to thermalization erasing the sensed information encoded in the NV quantum state distribution. If we assume a normalized readout SNR of 1 at the beginning of T_1 decay, a global initialization (via light-sheet) time of t_{init}^{LS}, a MW sequence time of t_{MW}, a single-voxel confocal readout time of t_{RO}^{conf}, and a beam movement dead-time of t_d, then η can be approximated as

$$\eta_{LC-QDM} = \underbrace{\frac{2}{1+e^{-1}}}_{\substack{\text{Avg. SNR between first} \\ \text{and last readout at } T_1}} \times \underbrace{\sqrt{\frac{(t_{init}^{LS} + t_{MW} + T_1)(t_{RO}^{conf} + t_d)}{T_1}}}_{\substack{\text{Avg. time required for} \\ \text{each recurrent readout}}}. \tag{2}$$

In comparison, the scanning QDM of Reference [30] does not have global NV initialization. Instead, after a global MW control sequence, a laser is applied to read out the NVs (lasting for t_{RO}^{conf}) and then to reinitialize them (lasting for t_{init}^{conf}) at each sensing voxel in a recurrent fashion until T_1 (**Figure 3a**). The per-voxel sensitivity from this protocol can be expressed as

$$\eta_{Leibold} = \frac{2}{1+e^{-1}} \times \sqrt{\frac{(t_{MW} + T_1)(t_{RO}^{conf} + t_{init}^{conf} + t_d)}{T_1}}. \tag{3}$$

For a conventional scanning QDM, only a single voxel is read out after initialization and a MW sequence. SNR is maximized for each NV sensing voxel by trading off time required for readout, resulting in per-voxel sensitivity given by

$$\eta_{conv} = \sqrt{t_{MW} + t_{RO}^{conf} + t_{init}^{conf} + t_d}. \tag{4}$$

3.3. LC-QDM performance comparison

We use the above measurements and expressions to estimate the relative per-voxel sensitivity of the LC-QDM to other scanning QDMs over a range of experimentally realistic values of t_{MW}, I_{LS}, and I_{conf} (**Figure 3b**). The maximum light-sheet intensity is assumed to be 2 mW/μm^2, which can be achieved with 2 W laser power and a light-sheet thickness of 10 μm and a lateral size of 100 μm. The minimum readout laser power is 2 μW, which could be required in imaging applications with live cells to reduce phototoxicity. The MW sequence duration depends on NV ensemble concentration [3], diamond material properties [48], and measurement protocols [1]; a range between 1 μs and 1 ms is chosen for the present performance comparison. A complete list of parameter choices is given in **Table 1**. For the parameter space used here, the LC-QDM provides the best per-voxel sensitivity due to the long NV T_1 and increased readout duty cycle. The LC-QDM outperforms a conventional scanning QDM by an order-of-magnitude due to the lack of recurrent readout for the latter. The improvement is modest (compared to Reference [30]) when the confocal readout laser intensity is close to the NV saturation intensity (~1 mW/μm^2, where $t_{RO}^{conf} \sim t_{init}^{conf}$). However, in the case of low laser intensity (~100 μW/μm^2, $t_{RO}^{conf} \ll t_{init}^{conf}$), the LC-QDM becomes increasingly

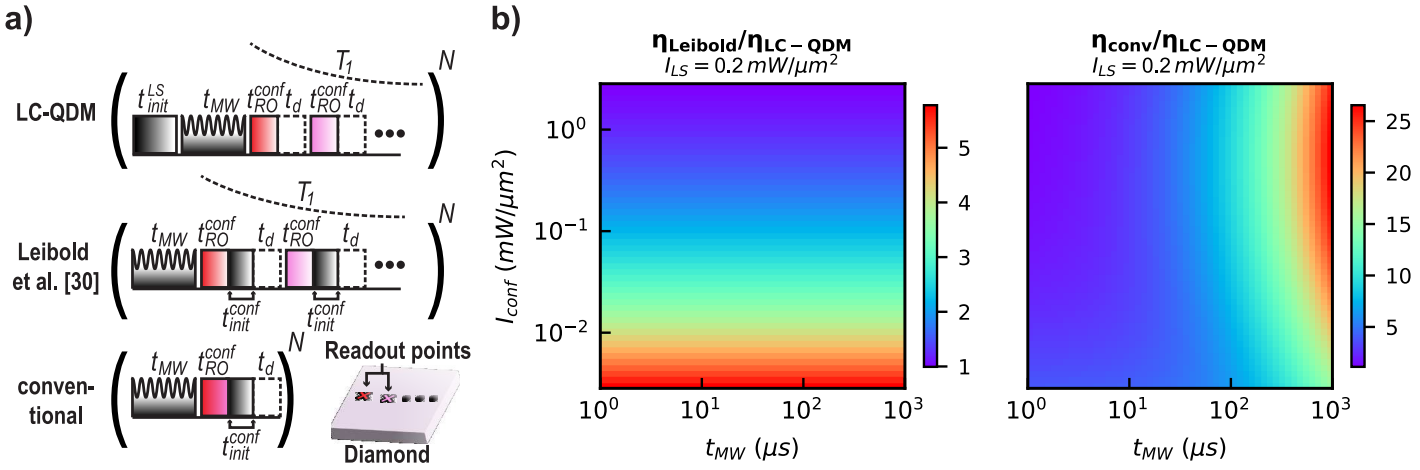


Figure 3 • Sensitivity comparison between LC-QDM, scanning QDM of Reference [30], and a conventional scanning QDM. (**a**) Schematic of measurement protocols employed in different QDMs. The LC-QDM employs global NV spin initialization, MW control, and recurrent local readout from as many spatial points as possible before T_1 limit. In comparison, Reference [30] utilizes global MW control with recurrent local readout and spin initialization and a conventional scanning QDM utilizes local MW control, initialization, and readout. See main text for details. (**b**) Calculation of relative per-voxel measurement sensitivity η as a function of readout laser intensity and MW pulse sequence duration, assuming $t_{init}^{LS} \approx t_{init}^{conf}$. Note that smaller η indicates a more sensitive measurement. Plots shown are for a fixed light-sheet intensity $I_{LS} = 0.2$ mW/μm^2. LC-QDM is projected to outperform the scanning QDM of Reference [30] and the conventional scanning QDM for nearly all experimental parameters simulated here.

Table 1 • Parameters used for comparison of relative per-voxel sensitivity shown in **Figure 3**.

Symbol	Description	Value
L_y	Light-sheet dimension in y direction	100 μm
d_{LS}	Light-sheet thickness	10 μm
P_{LS}	Laser power for light-sheet	2−2000 mW
I_{LS}	Intensity of light-sheet within Rayleigh range	$I_{LS} = \frac{P_{LS}}{L_y \times d_{LS}}$
δ_{conf}	Confocal readout laser beam diameter at focus	0.53 μm
P_{conf}	Laser power for confocal readout	2 μW (bioimaging)−2 mW
I_{conf}	Readout laser intensity within Rayleigh range	$I_{LS} = \frac{P_{LS}}{\delta_{conf}^2}$
t_{init}^{LS}	Spin initialization time at focus of light-sheet	**Figure 2c**
t_{init}^{conf}	Spin initialization time at focus of readout laser	**Figure 2c**
t_{RO}^{conf}	Spin readout time at focus of readout laser	**Figure 2d**
t_d	Dead time for steering readout laser and PL	100 ns
t_{MW}	MW sequence duration	1−1000 μs

advantageous, e.g., a 5 × improvement of per-voxel sensitivity corresponds to 25 × reduction of experimental time. We note that the behavior shown in **Figure 3b** remains nearly unchanged for all light-sheet intensities used in the modeling, as T_1 dominates over t_{init}^{LS} even for the weakest I_{LS}. Thus, the enhanced per-voxel sensitivity of the LC-QDM (Equation (2)) relative to the scanning QDM of Reference [30] (Equation (3)) arises primarily from differences between t_{RO}^{conf} and t_{init}^{conf}, as the readout duration has less dependence on laser intensity (see **Figure 2c,d**).

We also find that the relative per-voxel sensitivity of these QDM techniques has minimal dependence on NV concentration ([NV]), assuming optimized measurement protocol parameters. The concentration of NV centers in a diamond is typically related to the concentration of substitutional nitrogen impurities ([N]), as NV centers are formed through irradiation and annealing of nitrogen-doped diamond. Since [N] contributes significantly to NV spin dephasing and decoherence, it directly influences the MW pulse duration t_{MW}. By including t_{MW} as a sweep parameter in our analysis, we effectively provide a reference framework that accounts for variations in [NV], the interrogation sequence, and associated pulse durations. On the other hand, the initialization and readout times of NV centers are primarily determined by their optical transition dynamics and the applied laser intensity. Therefore, for a fixed illumination intensity, these times should exhibit minimal dependence on NV concentration, and the advantages of the LC-QDM are retained.

4. Conclusions

In this paper we outline the design, operation, and projected performance of the light-sheet confocal quantum diamond microscope (LC-QDM) to enable rapid readout of large NV sensor volumes while maintaining diffraction-limited resolution in 3D. The LC-QDM has two key features. First, a broad light-sheet is used for initialization of all NVs across a wide FOV. Second, a pair of AOMs steers the readout laser beam so that a fixed pinhole can reject out-of-focus light to achieve confocal resolution of NV PL. This inherent high-resolution readout obviates the need for diamond chips with thin NV layers or complex illumination beam shaping. Instead, a commercially available bulk NV-diamond chip can be used for efficient, widefield 3D quantum sensing with spatial resolution ∼1 μm. Decoupling NV spin initialization from readout is particularly advantageous for applications where readout laser power is limited, such as magnetic imaging of biological samples. The LC-QDM should be compatible with diverse NV measurement protocols [2, 19, 49], making it useful for a host of quantum sensing applications in areas such as material science, strain imaging, damage track detection, and bioimaging.

Acknowledgments

We thank Johannes Cremer, Connor Hart, Stephen DeVience, Mason Camp, Maximilian Shen, Jiarui Yu, Richard Escalante, and Andrew Beling for useful discussions.

Funding

This work is supported by, or in part by, the U.S. Army Research Laboratory, under Contract No. W911NF2420143; the U.S. Army Research Office, under Grant No. W911NF2120110; and the University of Maryland Quantum Technology Center.

Author contributions

Conceptualization, D.G.A. and J.T.; methodology, D.G.A. and J.T.; validation, D.G.A. and J.T.; formal analysis, D.G.A. and J.T.; writing—original draft preparation, D.G.A. and J.T.; writing—review and editing, D.G.A., J.T. and R.L.W.; supervision, D.G.A.

and R.L.W.; funding acquisition: R.L.W. All authors have read and agreed to the published version of the manuscript.

Conflict of interest

R.L.W. is a founder of and advisor to companies that are developing and commercializing NV sensing technology. These relationships are disclosed to and managed by the University of Maryland Conflict of Interest Office. These companies did not have any relationship with this study.

Data availability statement

Data supporting these findings are available within the article, at https://doi.org/10.20935/AcadQuant7690, or upon request.

Additional information

Received: 2025-03-01

Accepted: 2025-04-22

Published: 2025-04-30

Academia Quantum papers should be cited as *Academia Quantum 2025*, ISSN 3064-979X, https://doi.org/10.20935/AcadQuant7690. The journal's official abbreviation is *Acad. Quant*.

Publisher's note

Academia.edu Journals stays neutral with regard to jurisdictional claims in published maps and institutional affiliations. All claims expressed in this article are solely those of the authors and do not necessarily represent those of their affiliated organizations, or those of the publisher, the editors and the reviewers. Any product that may be evaluated in this article, or claim that may be made by its manufacturer, is not guaranteed or endorsed by the publisher.

Copyright

© 2025 copyright by the authors. This article is an open access article distributed under the terms and conditions of the Creative Commons Attribution (CC BY) license (https://creativecommons.org/licenses/by/4.0/).

References

1. Levine EV, Turner MJ, Kehayias P, Hart CA, Langellier N, Trubko R, et al. Principles and techniques of the quantum diamond microscope. Nanophotonics. 2019;8:1945–73. doi: 10.1515/nanoph-2019-0209

2. Tang J, Yin Z, Hart CA, Blanchard JW, Oon JT, Bhalerao S, et al. Quantum diamond microscope for dynamic imaging of magnetic fields. AVS Quantum Sci. 2023;5(11):044403. doi: 10.1116/5.0176317

3. Barry JF, Schloss JM, Bauch E, Turner MJ, Hart CA, Pham LM, et al. Sensitivity optimization for NV-diamond magnetometry. Rev Mod Phys. 2020;92(1):015004. doi: 10.1103/RevModPhys.92.015004

4. Ku MJH, Zhou TX, Li Q, Shin YJ, Shi JK, Burch C, et al. Imaging viscous flow of the Dirac fluid in graphene. Nature. 2020;583:537–41. doi: 10.1038/s41586-020-2507-2

5. Barry JF, Turner MJ, Schloss JM, Glenn DR, Song Y, Lukin MD, et al. Optical magnetic detection of single-neuron action potentials using quantum defects in dia-mond. Proc Natl Acad Sci USA. 2016;113(50):14133–8. doi: 10.1073/pnas.1601513113

6. Fescenko I, Laraoui A, Smits J, Mosavian N, Kehayias P, Seto J, et al. Diamond magnetic microscopy of malarial hemozoin nanocrystals. Phys Rev Appl. 2019;11:034029. doi: 10.1103/PhysRevApplied.11.034029

7. Davis HC, Ramesh P, Bhatnagar A, Lee-Gosselin A, Barry JF, Glenn DR, et al. Mapping the microscale origins of magnetic resonance image contrast with subcellular diamond mag-netometry. Nat Commun. 2018;9:131. doi: 10.1038/s41467-17-02471-7

8. Kazi Z, Shelby IM, Watanabe H, Itoh KM, Shutthanan-dan V, Wiggins PA, et al. Wide-field dynamic magnetic microscopy using double-double quantum driving of a diamond defect ensemble. Phys Rev Appl. 2021;15(5):054032. doi: 10.1103/PhysRevApplied.15.054032

9. Glenn DR, Fu RR, Kehayias P, Le Sage D, Lima EA, Weiss BP, et al. Micrometer-scale magnetic imaging of geological samples using a quantum diamond microscope. Geochem Geophys Geosyst. 2017;18:3254–67. doi: 10.1002/2017GC006946

10. Fu RR, Maher BA, Nie J, Gao P, Berndt T, Folsom E, et al. Pinpointing the mechanism of magnetic enhancement in modern soils using high-resolution magnetic field imaging. Geochem Geophys Geosyst. 2023;24:e2022GC010812. doi: 10.1029/2022GC010812

11. Mittelholz A, Steele SC, Fu RR, Johnson CL, Lillis RJ, Stucky de Quay G. Magnetic field signatures of craters on Mars. Geophys Res Lett. 2024;51:e2023GL106788. doi: 10.1029/2023GL106788

12. Taylor RJ, Reddy SM, Saxey DW, Rickard WD, Tang F, Borlina CS, et al. Direct age constraints on the magnetism of Jack Hills zircon. Sci Adv. 2023;9:eadd1511. doi: 10.1126/sci-adv.add1511

13. Turner MJ, Langellier N, Bainbridge R, Walters D, Meesala S, Babinec TM, et al. Magnetic field fingerprinting of integrated-circuit activity with a quantum diamond microscope. Phys Rev Appl. 2020;14(1):014097. doi: 10.1103/PhysRevApplied.14.014097

14. Lenz JN, 1. Perryman SK, Martynowych DJ, Hopper DA, Oliver SM. Hardware trojan detection potential and limits with the quantum diamond microscope. arXiv. 2024. arXiv:2402.08004

15. Oliver SM, Martynowych DJ, Turner MJ, Hopper DA, Walsworth RL, Levine EV. Vector magnetic current imaging of an 8 nm process node chip and 3D current distributions

using the quantum diamond microscope. Proceedings of the ASM International Symposium for Testing and Failure Analysis; 2021 Oct 31–Nov 4; Phoenix, AZ, USA. 2021. Vol. 84215, p. 96–107. doi: 10.31399/asm.cp.istfa2021p0096

16. Kehayias P, Levine EV, Basso L, Henshaw J, Ziabari MS, Titze M, et al. Measurement and simulation of the magnetic fields from a 555 timer integrated circuit using a quantum diamond microscope and finite-element analysis. Phys Rev Appl. 2022;17:014021. doi: 10.1103/PhysRevApplied.17.014021

17. Marshall MC, Turner MJ, Ku MJH, Phillips DF, Walsworth RL. Directional detection of dark matter with diamond. Quantum Sci Technol. 2021;6(2):024011. doi: 10.1088/2058-9565/abe5ed

18. Ebadi R, Marshall MC, Phillips DF, Cremer J, Zhou T, Titze M, et al. Directional detection of dark matter using solid-state quantum sensing. AVS Quantum Sci. 2022;4(11):044701. doi: 10.1116/5.0117301

19. Marshall MC, Ebadi R, Hart C, Turner MJ, Ku MJH, Phillips DF, et al. High-precision mapping of diamond crystal strain using quantum interferometry. Phys Rev Appl. 2022;17:024041. doi: 10.1103/PhysRevApplied.17.024041

20. Doherty MW, Manson NB, Delaney P, Jelezko F, Wrachtrup J, Hollenberg LCL. The nitrogen-vacancy colour centre in diamond. Phys Rep. 2013;528:1–45. doi: 10.1016/j.physrep.2013.02.001

21. Rietwyk KJ, Shaji A, Robertson IO, Healey AJ, Singh P, Scholten SC, et al. Practical limits to spatial resolution of magnetic imaging with a quantum diamond microscope. AVS Quantum Sci. 2024;6. doi: 10.1116/5.0230098

22. Broadway D, Lillie S, Scholten S, Rohner D, Dontschuk N, Maletinsky P, et al. Improved current density and magnetization reconstruction through vector magnetic field measurements. Phys Rev Appl. 2020;14(2):024076. doi: 10.1103/PhysRevApplied.14.024076

23. Roth BJ, Sepulveda NG, Wikswo JP Jr. Using a magnetometer to image a two-dimensional current distribution. J Appl Phys. 1989;65:361–72. doi: 10.1063/1.342549

24. Edmonds AM, Hart CA, Turner MJ, Colard PO, Schloss JM, Olsson KS, et al. Characterisation of CVD diamond with high concentrations of nitrogen for magnetic-field sensing applications. Mater Quantum Technol. 2021;1:025001. doi: 10.1088/2633-4356/abd88a

25. Thorlabs Inc. Single-Crystal Diamonds. [Cited 2025 Apr 20]. Available from: https://www.thorlabs.com/newgrouppage9 .cfm?objectgroup_id=15078

26. Tetienne JP, Broadway DA, Lillie SE, Dontschuk N, Teraji T, Hall LT, et al. Proximity-induced artefacts in magnetic imaging with nitrogen-vacancy ensembles in diamond. Sensors. 2018;18(4):1290. doi: 10.3390/s18041290

27. Ang DG, Liu X, Tang J, Shen M, Ebadi R, Walsworth R. Progress toward a solid-state directional dark matter detector. arXiv. 2024. arXiv:2405.01626. doi: 10.48550/arXiv.2405.01626

28. Gruber A, Dräbenstedt A, Tietz C, Fleury L, Wrachtrup J, v. Borczyskowski C. Scanning confocal optical microscopy and magnetic resonance on single defect centers. Science. 1997;276(5321):2012–4. doi: 10.1126/science.276.5321.2012

29. Nichols AJ, Evans CL. Video-rate scanning confocal microscopy and microendoscopy. J Vis Exp. 2011;(3252). doi: 10.3791/3252

30. Leibold JP, von Grafenstein NR, Chen X, Müller L, Briegel KD, Bucher DB. Time-space encoded readout for noise suppression and scalable scanning in optically active solid-state spin systems. arXiv. 2024. arXiv:2408.14894. doi: 10.48550/arXiv.2408.14894

31. Cambria M, Chand S, Kolkowitz S. Scalable parallel measurement of individual nitrogen-vacancy centers. arXiv. 2024. arXiv:2408.11715. doi: 10.48550/arXiv.2408.11715

32. Maurer PC, Maze JR, Stanwix PL, Jiang L, Gorshkov AV, Zibrov AA, et al. Far-field optical imaging and manipulation of individual spins with nanoscale resolution. Nat Phys. 2010;6(11):912–8. doi: 10.1038/nphys1774

33. Jaskula JC, Bauch E, Arroyo-Camejo S, Lukin MD, Hell SW, Trifonov AS, et al. Superresolution optical magnetic imaging and spectroscopy using individual electronic spins in diamond. Opt Express. 2017;25(11):11048–64. doi: 10.1364/OE.25.011048

34. Arai K, Belthangady C, Zhang H, Bar-Gill N, DeVience SJ, Cappellaro P, et al. Fourier magnetic imaging with nanoscale resolution and compressed sensing speed-up using electronic spins in diamond. Nat Nanotechnol. 2015;10(10):859–64. doi: 10.1038/nnano.2015.171

35. Räcke P, Pietzonka L, Meijer J, Spemann D, Wunder-lich R. Vacancy diffusion and nitrogen-vacancy center formation near the diamond surface. Appl Phys Lett. 2021;118(20): 204003. doi: 10.1063/5.0046031

36. Yamamoto T, Onoda S, Ohshima T, Teraji T, Watanabe K, Koizumi S, et al. Isotopic identification of engineered nitrogen-vacancy spin qubits in ultrapure diamond. Phys Rev B. 2014;90(8):081117. doi: 10.1103/PhysRevB.90.081117

37. Sage DL, Arai K, Glenn DR, DeVience SJ, Pham LM, Rahn-Lee L, et al. Optical magnetic imaging of living cells. Nature. 2013;496(7444):486. doi: 10.1038/nature12072

38. Olarte OE, Andilla J, Gualda EJ, Loza-Alvarez P. Light-sheet microscopy: a tutorial. Adv Opt Photonics. 2018;10(1):111–79. doi: 10.1364/AOP.10.000111

39. Eisenach ER, Barry JF, Pham LM, Rojas RG, Englund D, Braje DA. Broadband loop gap resonator for nitrogen vacancy centers in diamond. Rev Sci Instrum. 2018;89(9):094705. doi: 10.1063/1.5037465

40. Horsley A, Appel P, Wolters J, Achard J, Tallaire A, Maletinsky P, et al. Microwave device characterization using a widefield diamond microscope. Phys Rev Appl. 2018;10(4):044039. doi: 10.1103/PhysRevApplied.10.044039

41. Laissue PP, Alghamdi RA, Tomancak P, Reynaud EG,

Shroff H. Assessing phototoxicity in live fluorescence imaging. Nat Methods. 2017;14(7):657–61. doi: 10.1038/nmeth.4344

42. Xu F, Chen J, Hou Y, Cheng J, Hui TK, Chen SC, et al. Super-resolution enabled widefield quantum diamond microscopy. ACS Photonics. 2024;11(1):121–7. doi: 10.1021/acsphotonics.3c01077

43. Waxman A, Schlussel Y, Groswasser D, Acosta VM, Bouchard LS, Budker D, et al. Diamond magnetometry of superconducting thin films. Phys Rev B. 2014;89(5):054509. doi: 10.1103/PhysRevB.89.054509

44. Acosta VM, Bouchard LS, Budker D, Folman R, Lenz T, Maletinsky P, et al. Color centers in diamond as novel probes of superconductivity. J Supercond Nov Magn. 2019;32(1):85–95. doi: 10.1007/s10948-018-4877-3

45. Danda G, Masih Das P, Drndic M. Laser-induced fabrication of nanoporous monolayer WS2 membranes. 2D Mater. 2018;5(3):035011. doi: 10.1088/2053-1583/aabb73

46. Kotsakidis JC, Zhang Q, Vazquez de Parga AL, Currie M, Helmerson K, Gaskill DK, et al. Oxidation of monolayer WS2 in ambient is a photoinduced process. Nano Lett. 2019;19(8):5205–15. doi: 10.1021/acs.nanolett.9b01599

47. Volkova K, Kumar AM, Bolotin K, Naydenov B. A glovebox-integrated confocal microscope for quantum sensing in inert atmosphere. Rev Sci Instrum. 2025;96(1):013703. doi: 10.1063/5.0244999

48. Bauch E, Singh S, Lee J, Hart CA, Schloss JM, Turner MJ, et al. Decoherence of ensembles of nitrogen-vacancy centers in diamond. Phys Rev B. 2020;102(13):134210. doi: 10.1103/PhysRevB.102.134210

49. Glenn DR, Bucher DB, Lee J, Lukin MD, Park H, Walsworth RL. High-resolution magnetic resonance spectroscopy using a solid-state spin sensor. Nature. 2018;555(7698):351–4. doi: 10.1038/nature25781